Smart Materials in Manufacturing 2 (2024) 100048

Contents lists available at ScienceDirect

Smart Materials in Manufacturing

journal homepage: www.keaipublishing.com/en/journals/smart-materials-in-manufacturing

Research Paper

Broadening the microstructure regime of Al_2O_3–ZrO_2 hypereutectic ceramic fabricated via laser powder bed fusion

Kai Zhang [a,*], Shurui Li [a], Tingting Liu [a,**], Zhiwei Xiong [a], Zhiguang Zhu [a], Yang Zhang [a], Abid Ullah [b,c], Wenhe Liao [a]

[a] *School of Mechanical Engineering, Nanjing University of Science and Technology, Nanjing, 210094, China*
[b] *Centre for Additive Manufacturing, School of Engineering, RMIT University, Melbourne, VIC, 3000, Australia*
[c] *Institute of Laser and System Technologies, Hamburg University of Technology, Hamburg, 21079, Germany*

ARTICLE INFO

Keywords:
Laser powder bed fusion
Al_2O_3–ZrO_2
Microstructure
Hypereutectic structure
Eutectic structure

ABSTRACT

The microstructure and mechanical property regime of laser powder bed fusion fabricated Al_2O_3–ZrO_2 hypereutectic ceramic samples were thoroughly investigated by tailoring the printing parameters. The findings indicate that both the hypereutectic and eutectic microstructure are obtained depending on the varying printing parameters. The ZrO_2 dendrites in the hypereutectic structure gradually refine as the laser energy density increases, while the surrounding eutectic structure evolves continuously. The uniform eutectic microstructure is developed until the dendrites disappear. Simultaneously, it is observed that coarse Al_2O_3 particles were formed in the overlap part of the eutectic structure where the laser energy is higher. In terms of mechanical properties, the samples with alumina particles in the eutectic microstructure have a maximum hardness of 1616.13 HV, while the sample with uniform eutectic microstructure has the highest fracture toughness of 5.87 MPa·m$^{1/2}$. These findings can contribute to the introduction of a unique microstructure in Al_2O_3–ZrO_2 ceramic.

1. Introduction

Al_2O_3–ZrO_2 composite ceramics combine the high strength of Al_2O_3 concurrent with the good toughness of ZrO_2, resulting in excellent mechanical properties across a wide temperature range, including room and elevated temperatures. As advanced high temperature structural materials, they possess great potential for usage in high performance aero-engines and heavy-duty gas turbines. Traditional sintering processes of Al_2O_3–ZrO_2 ceramics such as spark plasma sintering (SPS) [1,2], microwave-assisted sintering [3], and oscillatory pressure sintering [4] have proven to be effective methods for achieving uniform microstructures [5,6]. In contrast, solidification techniques of Al_2O_3–ZrO_2 ceramics such as micro-pulling down [7], Bridgman [8], floating zone (FZ) [9,10], and laser-based additive manufacturing (AM) technologies [11–14] have resulted in unique interwoven and interspersed microstructures [15]. In recent years, these melt solidification methods have attracted considerable interest in studying the microstructural evolution of AM parts [16–22].

In the domain of advanced ceramic manufacturing, laser-based AM technologies, including laser powder bed fusion (L-PBF) and direct energy deposition (DED), have shown promise for the fabrication of Al_2O_3–ZrO_2 ceramics because they can overcome the material's high melting temperature to achieve fine and uniform microstructures apart from fabricating intricate-shaped components [23–27]. To date, most of the research focuses on the DED technology [28,29] to fabricate ceramic components. Su et al. [30–33] investigated the large-scale Al_2O_3/$GdAlO_3$/ZrO_2 ternary eutectic ceramic rod by laser DED, where the colonies and banded structures were restrained by heat treatment. Moreover, the most critical influencing factor of periodic strip thickness is the feeding rate. Subsequently, the process was optimized and improved using ultrasonic, which resulted in a desirable surface morphology. Wu et al. [34] found the periodic banded structure in the laser-engineered net shaping (LENS) fabricated Al_2O_3–ZrO_2 eutectic ceramic, which affects microstructure uniformity. Besides, the formation, evolution, and elimination of cracks during the ceramic fabrication process were investigated [35]. In comparison to the research work conducted on ceramics fabrication using DED, there has been minimal investigation into fabricating Al_2O_3–ZrO_2 ceramics via L-PBF.

---

[*] Corresponding author.
[**] Corresponding author.
E-mail addresses: zhangkai@njust.edu.cn (K. Zhang), liutingting@mail.njust.edu.cn (T. Liu).

https://doi.org/10.1016/j.smmf.2024.100048
Received 1 December 2023; Received in revised form 22 February 2024; Accepted 22 February 2024

In terms of composition, the eutectic composition has been extensively studied for its industrial relevance and unique properties, including good thermal stability and mechanical properties. Whereas the hypoeutectic and hypereutectic regions have drawn less attention. However, investigating the solidification behavior of Al_2O_3–ZrO_2 ceramics with a broader compositional landscape is essential to understand the "composition-microstructure" correlation during L-PBF and, consequently, to customize the mechanical properties. Wu et al. [36,37] fabricated melt-grown Al_2O_3–ZrO_2 hypoeutectic, eutectic, and hypereutectic ceramics using DED technology. The study shows that a large number of hypereutectic microstructures were observed on functionally graded ceramics. However, only the compositional dependence on the microstructure evolution is studied and the influence of laser parameters on the evolution of hypereutectic microstructure is overlooked. Specifically, it is noteworthy that the full eutectic lamellar microstructure was obtained for the hypereutectic $Al_2O_3/Y_3Al_5O_{12}/ZrO_2$ ceramic fabricated by the laser floating zone [38]. However, the detailed mechanism has not been discussed. Subsequently, a homogeneous and crack-free ternary nanostructured Al_2O_3/YAG/ZrO_2 hypereutectic plate with a large surface is successfully produced by laser remelting [39]. The obtained results indicate that, under the same growth conditions, the interphase spacing of ternary hypereutectic is much smaller than that of ternary eutectic composition.

Evidently, there is still a gap in fabricating and understanding the microstructure evolution of Al_2O_3–ZrO_2 hypereutectic ceramics via L-PBF. Based on the Al_2O_3–ZrO_2 binary phase diagram, it is obvious that both ZrO_2 content and temperature have a significant impact on the microstructure evolution. Therefore, two different hypereutectic compositions were used, and the resultant hypereutectic microstructures were analyzed to investigate the microstructure evolution mechanisms. In addition, the scanning speeds were set as the variables to broaden the microstructure regime of L-PBF fabricated Al_2O_3–ZrO_2 hypereutectic ceramics as well as their mechanical properties, including hardness and fracture toughness.

2. Materials and methods

2.1. Sample preparation

CT3000-SG Al_2O_3 powders (obtained from Qingdao Almatis Co. Ltd., Qingdao, China, average particle size of 410 nm) and XD-1024-3 ZrO_2 powders (supplied from MCC Xindun Co. Ltd., Shanghai, China, average particle size of 273 nm) were the commercially available raw powders used in the present work. According to the eutectic ratio of Al_2O_3–ZrO_2 (58.5 wt %: 41.5 wt %), two hypereutectic ratios used in this research are 35 wt %: 65 wt % and 25 wt %: 75 wt %, respectively. We refer to 'Z65' as the mass fraction of 65% ZrO_2 and 'Z75' as the mass fraction of 75% ZrO_2.

The slurry (ceramic paste) was used for the experiments during the L-PBF process, which ensures proper deposition of powder layers due to good flowability. The QM-3SP4 planetary ball mill (QM-3SP4, Guangzhou, China) was used at room temperature at a rotation speed of 150 rpm for 1 h. In this process, deionized water was used as the liquid media and mixed with the powder mixture in a ratio of 1 : 8 (wt: wt). The milling mode was 5 min of ball milling followed by a 1 min interval time. After wet grinding, the slurry suitable for the experiment was obtained.

The printing process was carried out using an in-house developed L-PBF system. The system was equipped with an IPG YLR-500 single-mode continuous wave fiber laser operating at a wavelength of 1064 nm with a maximum power of 500 W. Prior to initiating the process and directing the laser upon the powder, the Al_2O_3 substrate was fixed and leveled onto the build platform. The slurry was uniformly distributed over the substrate with the help of the mounted movable scraper, and then the slurry was dried and preheated by induction heating during the experiment, and the handheld hot air gun was aimed at the slurry powder layer and dried at 200 °C for 30 s to evaporate the moisture. After obtaining the dried powder bed, the laser scans and melts the selected area to complete the printing of one layer, and then the substrate descends a layer thickness distance (50 μm) with the work platform, and the laying slurry, drying, and printing are repeatedly completed, and finally, the formed block part is obtained.

A zig-zag type scanning strategy was used for the layer-by-layer fabrication of Al_2O_3–ZrO_2 hypereutectic ceramics. According to the previous reports [40,41] and research results by this lab, in order to obtain better forming quality to study the law of tissue evolution, the processing parameters for ceramics used in the experiment were as follows: laser power of 70 W and 90 W, scanning speeds of 40 mm/s - 120 mm/s with intervals of 20 mm/s, a layer thickness of 50 μm, scanning space of 100 μm, and the laser scanning path was rotated by 90° between adjacent layers. A schematic of the process is shown in Fig. 1.

2.2. Microstructure characterization

Phase formation of the powders and prepared samples were analyzed using an X-ray diffractometer (XRD, Bruker-AXS D8 Advance, Bruker, Germany). The analysis was performed using Cuk_α radiation with a current of 40 mA and voltage of 40 kV, at a scanning rate of 1°/min. The results were qualitatively analyzed using MDI Jade 6.0 software and the Inorganic Crystal Structures Database (ICSD) to obtain the phase formation in the printed samples. Due to the non-conductivity of the Al_2O_3–ZrO_2 sample, a platinum conductive film underwent coating on the sample surface using plasma sputtering (Leica ACE 200). The surface morphology and microstructure of the samples were examined using a field emission scanning electron microscope (SEM, FEI Quanta 250F, America) equipped with an energy dispersive spectrometer (EDS, Oxford Instruments, United Kingdom).

Hardness and fracture toughness measurements were conducted on the cross-sectional surfaces of the samples following the polishing process. Vickers hardness tester (HVS-1000Z, Shanghai Microcre Light-Mach Tech Co. Ltd., China) was conducted with a loading force of 9.8 N and a dwelling time of 10 s. Five indentations were randomly conducted on the surface of each sample. The fracture toughness of samples was measured by the micro indentation method. An optical microscope (OM, VK-X4, Keyence) and ImageJ software were used to measure the diagonal length of indentation and crack length produced by indentation corners. Vickers hardness (HV) is calculated by Eq. (1), and then fracture toughness (K_{IC}) is estimated by Eq. (2).

$$HV = \frac{P}{F} = 1.8544\frac{P}{(2a)^2} \tag{1}$$

$$K_{IC} = 0.016\left(\frac{E}{HV}\right)^{1/2}\frac{P}{c^{3/2}} \tag{2}$$

where P is the loading force (N), F is the indentation area (mm^2), a is half the length of the indentation diagonal (mm), c is the half length of the crack (mm), and E is elastic modulus (GPa). To calculate the fracture toughness using Eq. (2), the elastic modulus of the Al_2O_3–ZrO_2 is needed for substituting into the equation. In this paper, the elastic modulus of composites (E_C) was calculated by Halpin–Tsai equation [37]:

$$E_C = E_{Al_2O_3} f_{Al_2O_3} + E_{ZrO_2} f_{ZrO_2} \tag{3}$$

where $E_{Al_2O_3}$ is the elastic modulus of Al_2O_3, E_{ZrO_2} is the elastic modulus of ZrO_2, $f_{Al_2O_3}$ is the volume fraction of Al_2O_3, f_{ZrO_2} is volume fraction of ZrO_2. The specific values are shown in Table 1.

A thin slice or lamella is obtained from the sample through FIB milling (Helios G4 UX). The lift-out method involves transferring and attaching this slice onto a Transmission Electron Microscopy (TEM) grid. This allows for further analysis of the slice under TEM. A Transmission Electron Microscope with an acceleration voltage of 200 kilovolts (kV) is used for the structural investigation of interfaces. The FEI Talos F200X is

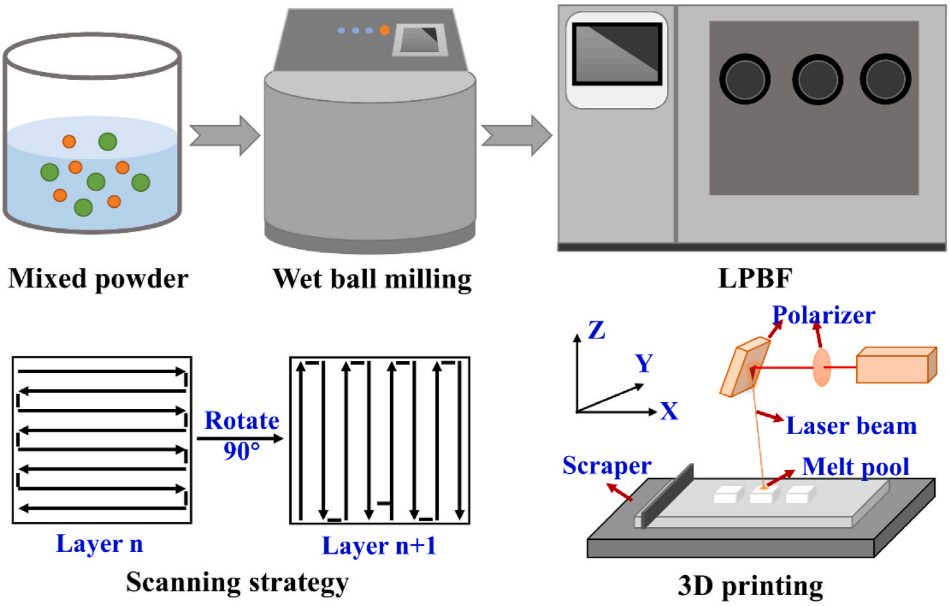

Fig. 1. The schematic diagram of the Al_2O_3–ZrO_2 eutectic ceramic samples preparation process.

Table 1
Elastic modulus [37] and volume fraction of the component phases.

Composition phase	Elastic modulus (E, GPa)	Volume fraction (f, %)	
		Z65	Z75
Al_2O_3	390	24.37	16.63
ZrO_2	220	75.63	83.37

a specific model of TEM used in this study. The crystal orientation of the sample is investigated using Transmission Kikuchi Diffraction (TKD).

3. Results

3.1. Morphology of initial powder

The experiments were carried out using CT3000 SG grade Al_2O_3 powder with irregular flakes as shown in Fig. 2a. XD 1024-3 type ZrO_2 is smaller in particle size (~273 nm) and has almost spherical shape, as shown in Fig. 2b. The mixed powder was obtained after wet milling (Fig. 2c). Nanoscale ZrO_2 powder could be seen sticking to the surface of the irregular flakes Al_2O_3 powder. Elemental analysis was performed on the mixed powder, and EDS mapping of each element was obtained, as shown in Fig. 2d–f.

3.2. Phase and microstructure

To investigate the phase evolution of the hypereutectic Al_2O_3–ZrO_2 ceramic, XRD analyses were performed on the mixed powders and Z65 samples. According to Fig. 3a, the mixed powders solely displayed the monoclinic phase of ZrO_2 (m-ZrO_2) and Al_2O_3 (α-Al_2O_3), indicating that there is no phase transition caused by ball milling. However, after the L-PBF process, the m-ZrO_2 transformed to the stabilized tetragonal ZrO_2 (t-ZrO_2) which might have occurred due to temperature variations. The transformation from m-ZrO_2 to t-ZrO_2 typically occurs at temperatures between 1100 °C and 1200 °C, and it appears that the temperature during the L-PBF process exceeds this threshold. During the cooling process, t-ZrO_2 typically reverts to m-ZrO_2 from 1000 °C to 850 °C.

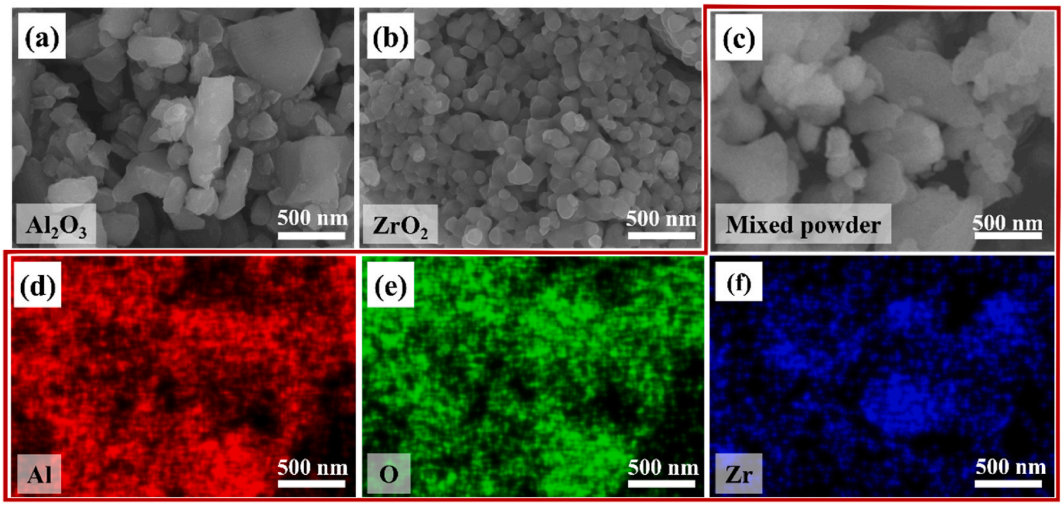

Fig. 2. SEM micrograph of starting powders: (a) Al_2O_3, (b) ZrO_2, (c) Al_2O_3–ZrO_2 powder after milling, (d) EDS mapping of Al element in mixed powder (figure c), (e) EDS mapping of O element in mixed powder (figure c), (f) EDS mapping of Zr element in mixed powder (figure c).

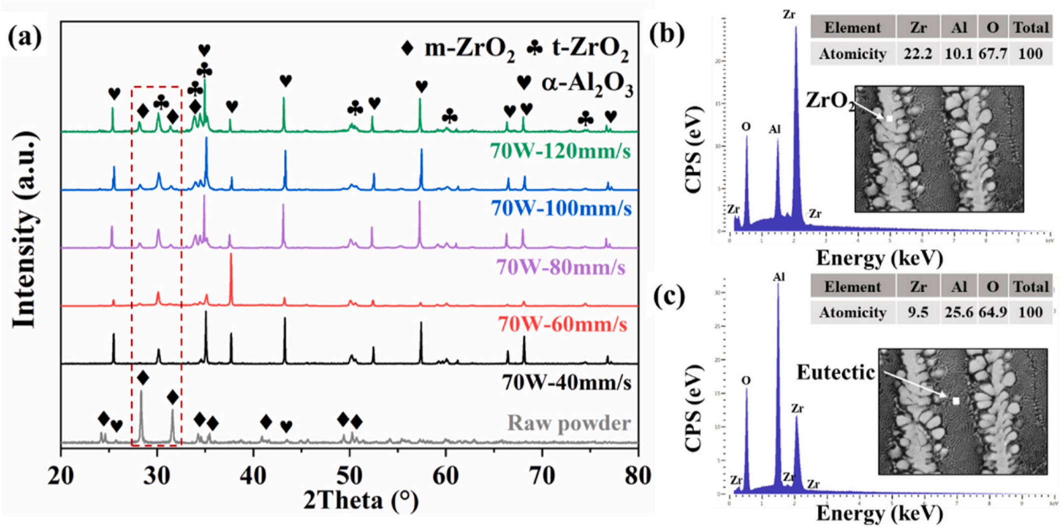

Element	Zr	Al	O	Total
Atomicity	22.2	10.1	67.7	100

Element	Zr	Al	O	Total
Atomicity	9.5	25.6	64.9	100

Fig. 3. (a) XRD patterns obtained from the mixture powder and Z65 samples, EDS analysis performed on (b) the white zone and (c) the grey zone of the Z65-70W-100 mm/s sample.

However, the XRD patterns showed a stable presence of t-ZrO_2. This preservation of the metastable t-ZrO_2 phase may be attributed to the inhibition of the martensitic transformation of t-ZrO_2 to m-ZrO_2 due to insufficient thermal equilibrium time and energy caused by the rapid cooling rate [42].

As depicted by the red dashed rectangular outline in Fig. 3a, the presence of the monoclinic phase (m-ZrO_2) was still apparent and the intensity of its peak increased with increasing scanning speed. This implies that higher scanning speeds lead to faster cooling rates and an increased concentration of m-ZrO_2, which is inconsistent with the

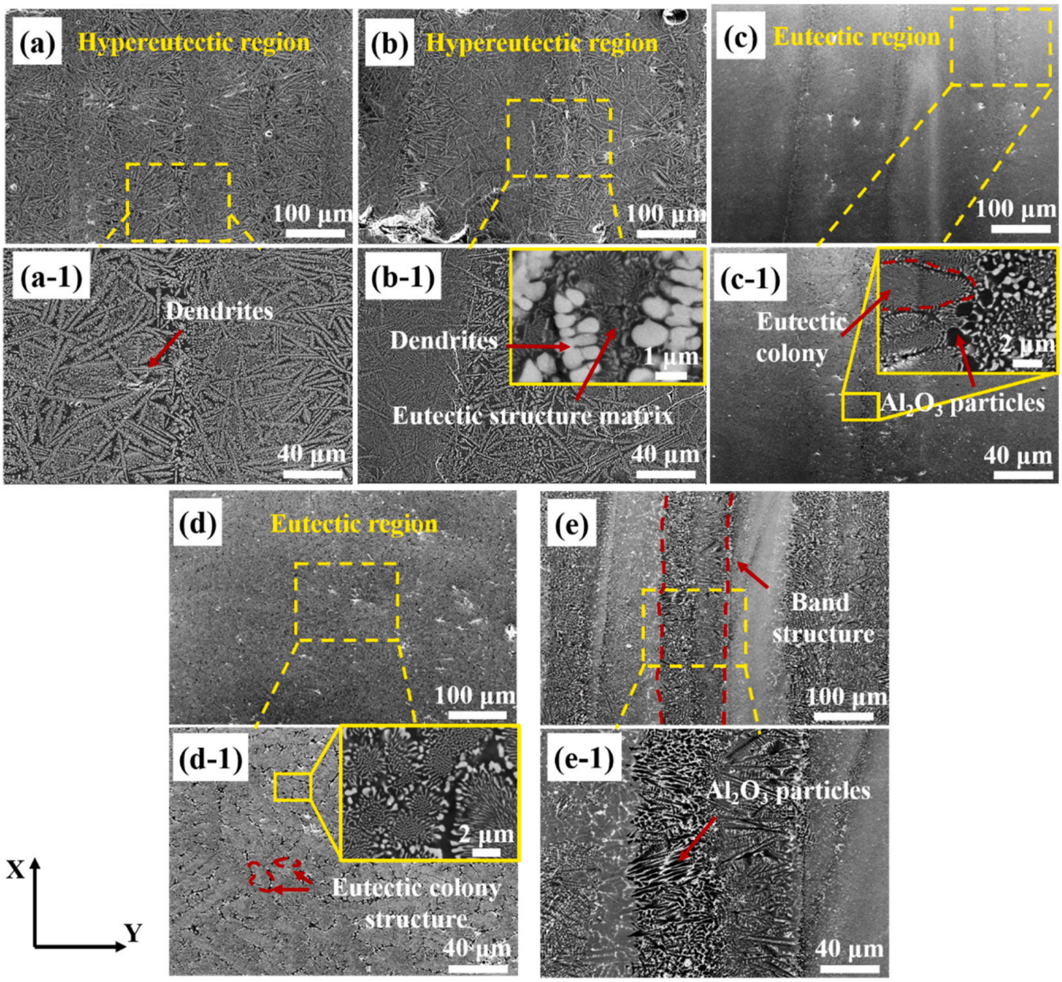

Fig. 4. SEM micrograph of Z65 samples in 70 W laser power: (a, a-1) 120 mm/s, (b, b-1) 100 mm/s, (c, c-1) 80 mm/s, (e, e−1) 60 mm/s, (f, f-1) 40 mm/s.

mechanism of t-ZrO_2 conversion to m-ZrO_2. Therefore, it is assumed that the detected m-ZrO_2 peaks in the samples represent the original m-ZrO_2 which has not transformed into the tetragonal phase and remains in its original state. A lower laser energy resulting from the high scanning speed induces inadequate melting of m-ZrO_2. Combining the XRD pattern with the EDS results (Fig. 3b and c), it can be observed that the white phase corresponds to ZrO_2, while the grey region represents the eutectic structure in the hypereutectic microstructure.

Fig. 4 illustrates the cross-sectional microstructural properties of Z65 samples with 70 W laser power at various scanning speeds. At high scanning speeds 120 mm/s and 100 mm/s, with a lower laser energy density, the samples exhibit a typical hypereutectic morphology consisting of the eutectic structure matrix and discrete ZrO_2 dendrites (Fig. 4a, a-1, b and b-1). That shows an inadequate energy input, lower melting, and faster cooling rates, all of which lead to the formation of dendrites and powder elongation. At 80 mm/s (Fig. 4c and c-1), the sample forms a compact eutectic colony structure and shows the presence of Al_2O_3 particles. This indicates that the optimum melting shown in Fig. 4c and c-1 produced a rather smooth surface morphology. At 60 mm/s, the sample shows an almost uniform and homogeneous eutectic colony structure, with no Al_2O_3 particles or ZrO_2 dendrites (Fig. 4d and d-1). At the process parameter of 40 mm/s, the sample exhibits a distinct band structure with a width of 107.5 ± 8.7 μm, consisting of a significant amount of Al_2O_3 particle structure (Fig. 4e and e−1) [29]. Figs. 4d–1 to e−1 show over melting of the powder and a slower cooling rate, which in some way caused the particles to evaporate and resulted in the formation of keyholes and surface roughness. This means that the energy intake is responsible for the formation of these structures, and as the laser energy density increases, the microstructure gradually transforms from a hypereutectic structure to a eutectic structure. Furthermore, comparing Fig. 4a–1 and e−1 reveals that Al_2O_3 particles have directional growth characteristics, whereas ZrO_2 dendrites lack such characteristics.

Apart from influencing the phase formation, the laser energy density also affects the morphology. As observed in the 40 mm/s sample (Figs. 4e–1), high laser energy densities result in the formation of Al_2O_3 particle structures, leading to microstructural heterogeneity. It is important to note that all Z65 samples were formed in the same experimental batch, ensuring uniformity of powder raw materials and experimental conditions. Therefore, the microstructure evolution can be attributed to the change in laser energy density.

Similar experimental results can also be observed for the Z75 samples. Fig. 5 shows the microstructural characteristics in cross section of Z75 samples at different scanning speeds. As same with Z65, the typical hypereutectic structure is formed when the laser energy density is low, and the microstructure evolved into eutectic structure with the laser energy density increases. The trend of decreasing ZrO_2 dendrites can be observed. The difference is that the microstructure is completely transformed into the eutectic structure when the scanning speed is reduced to 60 mm/s in Z75, while it is already transformed when the scanning speed is 80 mm/s in Z65. Therefore, more details about the evolution of hypereutectic structure can be observed in Z75 120-80 mm/s samples.

Higher magnifications of various sections are displayed in Fig. 6a to explore the band structure of the Z65-70W-40 mm/s sample, which plainly reveals that zone b is located within the band region. The coarsening band region is formed by the coarsening eutectic structure

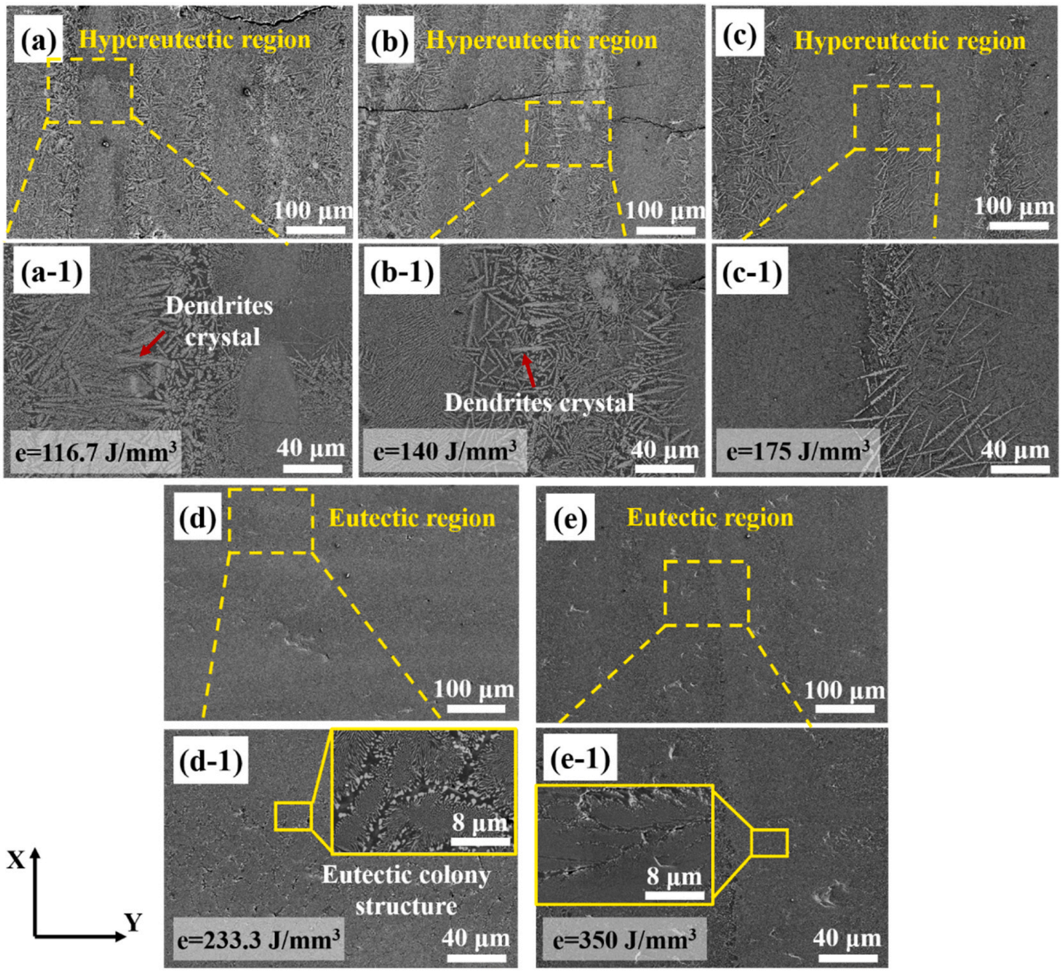

Fig. 5. SEM micrograph of Z75 samples: (a, a-1) 70 W-120 mm/s, (b, b-1) 70 W-100 mm/s, (c, c-1) 70 W-80 mm/s, (d, d-1) 70 W-60 mm/s, (e, e−1) 70 W-40 mm/s.

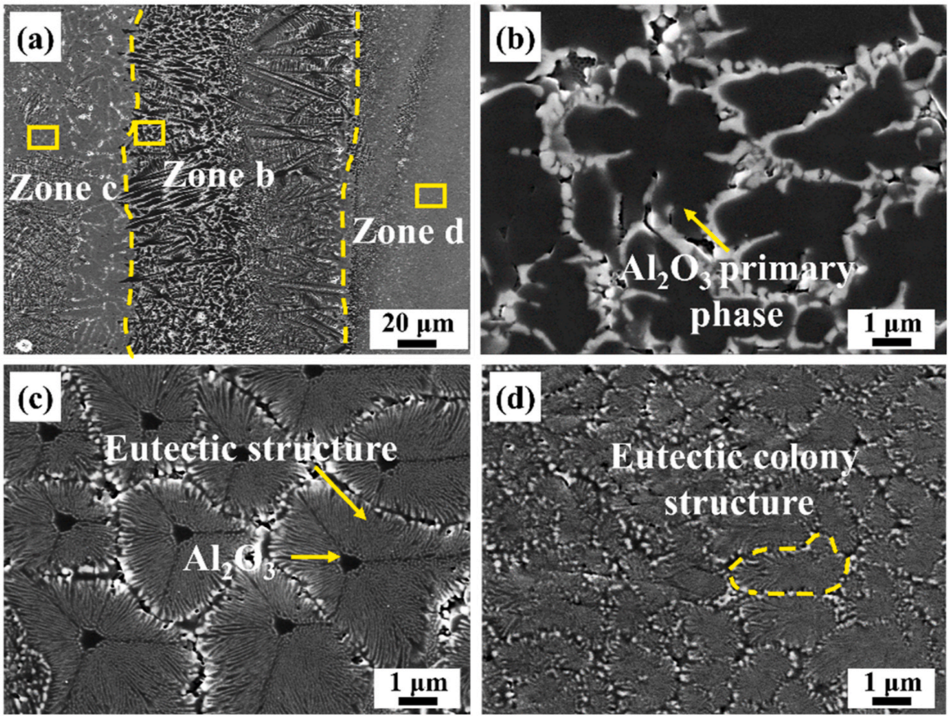

Fig. 6. SEM micrograph of Z65 hypereutectic ceramic samples 70 W-40 mm/s: (a) low magnification, (b) Zone b, (c) Zone c, (d) Zone d.

surrounding independent nucleation Al_2O_3 particles which exhibit a "Chinese script" [43–45] and "rod-like" structure (Fig. 6b). The microstructure of zone c consists of the eutectic structure and small Al_2O_3 particles. Compared to zone b, the size of the Al_2O_3 particles in zone c is significantly smaller and they are surrounded by the eutectic matrix, forming a mushroom-like structure (Fig. 6c). The microstructure of zone d shows a typical eutectic colony structure (Fig. 6d). In particular, zone b, which is located at the melt pool boundary, is affected by thermal effects [46,47] resulting from the overlap between the adjacent tracks. This increases the instability of the solid-liquid interface, resulting in the band structure observed in the sample [29,44,48]. A detailed demonstration of the microstructure evolution is given in Section 4.3.

Fig. 7 shows the microstructural morphology of the Z75 70 W-40 mm/s and 70 W-60 mm/s samples. The microstructure of the 70 W-40 mm/s sample shows a eutectic colony structure consisting of discrete ZrO_2 particles and a continuous Al_2O_3 matrix (Fig. 7a). At the boundary of the eutectic colony, cracks and cavities are occasionally observed, as shown in Figs. 7a–1. This is mainly due to the fact that precipitation from the liquid in the boundary region is considered to be the final stage of solidification. When the liquid is insufficient, the material in the boundary region cannot fill the space, resulting in the formation of cracks. Eutectic structures are composed of alternating components, and

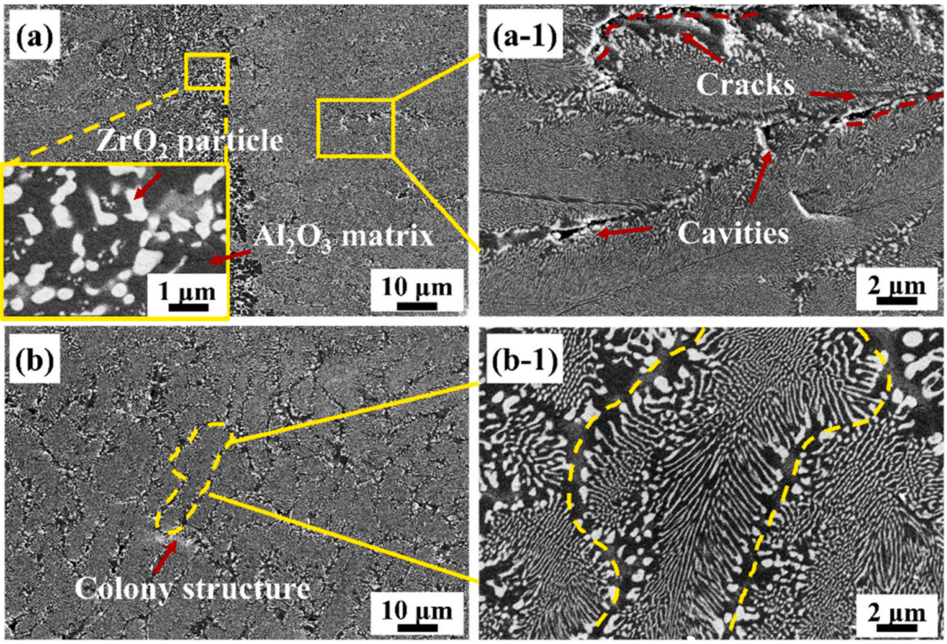

Fig. 7. SEM micrograph of Z75 samples at low and high magnification: (a, a-1) 70 W-40 mm/s, (b, b-1) 70 W-60 mm/s.

the solidification of the liquid phase causes significant shrinkage, thereby increasing the risk of cracks and cavity defect formation [46]. Concerning the microstructure of the 70 W-60 mm/s sample, it also exhibits a eutectic colony structure, as shown in Fig. 7b. As can be observed, for the colony structure of Al_2O_3–ZrO_2 eutectic, the center of colony is homogeneous and fine, while the boundary is coarse (Figs. 7b–1). The eutectic structure will not be described in detail in this paper, and more information is expounded in the previous research results.

Fig. 8 and Fig. S1 shows the microstructure of hypereutectic ceramics of Z75 samples fabricated at 70 W laser power, with 120 mm/s, 100 mm/s, and 80 mm/s scanning speed respectively. SEM and EDS were performed on several samples to analyze the evolution of hypereutectic microstructure. By combining EDS mapping and XRD pattern analysis (Fig. 3), it is evident that the hypereutectic morphology consists of t-ZrO_2 dendrites surrounded by eutectic structures.

Fig. 8a and b shows that t-ZrO_2 transforms from coarse primary dendrites to slender dendrites as the scanning speed decreases. At the same time, it is observed that the lamellar eutectic surrounding the t-ZrO_2 dendrites has no obvious boundary at scanning speed of 120 mm/s, and the t-ZrO_2 dendrites are discretely deposited in the lamellar eutectic matrix in primary form, as shown in a partial enlargement of Fig. 8a. At 100 mm/s, the eutectic structure gradually evolved into a cell shape surrounding the t-ZrO_2 dendrites (circled in red in Figs. 8b–2). The cell size was small and densely distributed around the dendrites (Figs. 8b–2). Comparing with Figs. 8b–2 and c, it can be found that the eutectic cells grew from 1.8 ± 0.23 μm to 5.2 ± 1.55 μm, as the scanning speed decreased. The cell size was measured by the analysis software Image J. It is obviously observed that the peripheral branches of the dendrite structure have disappeared by comparing Figs. 8b–2 and the partial enlargement of Fig. 8c. The eutectic cells are arranged along the growth direction of the ZrO_2 dendrite, and the long axis of the eutectic cells are perpendicular to the direction of the dendritic trunk. Moreover, the elongated dendrites were not completely disappeared in the center of the eutectic cells (red arrow in Fig. 8c). There are large dendrite arms/branches which are caused by increasing scanning speed. Increasing the scanning speed increases the maximum cooling rate and produces interface instabilities in the side of the cells that cause the growth of dendrite arms. The spacing between the cells increases and constitutional undercooling occurs perpendicular to the growth direction because of the higher scanning speed and lower temperature gradient. The result revealed the evolution process of the growth of small-size eutectic cells into large-size rod-shaped eutectic. In fact, the evolution of hypereutectic microstructure at different scanning speeds is essentially influenced by the change in laser energy density. More detail about this is demonstrated in Section 4.2.

To further reveal the phase structure of the ZrO_2 dendrites in the Al_2O_3–ZrO_2 hypereutectic ceramic, the transmission electron microscopy (TEM) technique was employed and the results are shown in Fig. 9. Fig. 9b displays the bright-field TEM image and corresponding selected area electron diffraction (SAED) pattern of the ZrO_2 dendrite main trunk region (labeled as region b in Fig. 9a). The crystal plane spacing measured from the SAED pattern correspond to different crystallographic planes of m-ZrO_2, such as 0.478 nm $|(100)|$ (d_{std} = ~0.5078 nm), 0.318 nm $|(-111)|$ (d_{std} = ~0.3163 nm), 0.25 nm $|(-102)|$ (d_{std} = ~0.2498 nm). From Fig. 9b, it can be observed that the ZrO_2 dendrites are surrounded by Al_2O_3. Further insight into the interface relationship between the ZrO_2 dendrites and the Al_2O_3 matrix can be obtained from the high-resolution TEM (HRTEM) image of the interface region in Fig. 9c. The study reveals that the crystal orientation parallelism between ZrO_2 and Al_2O_3 was not observed, and the ZrO_2 lattice is axisymmetric, which indicates the presence of twins in the ZrO_2 crystal. Fig. 9d presents the bright-field TEM image and corresponding SAED pattern of the ZrO_2 dendrite side branch region (labeled as region d in Fig. 9a). By combining the energy-dispersive X-ray spectroscopy (EDXS) mapping in Fig. 9e, it can be observed that the side branch is enveloped by an approximately 89.8 ± 15.27 nm thick layer of Al_2O_3, which is deposited within the eutectic matrix. Additionally, the lattice of the side branch is consistent with that of the main trunk region, indicating that the entire ZrO_2 dendrite exhibits a monoclinic phase with a p21/c space group structure. Finally, Fig. 9f shows the HRTEM image of region f in Fig. 9d, where evident layer mismatches are observed at the twin boundaries within the ZrO_2 dendrite.

3.3. *Mechanical properties*

The Vickers hardness values were measured on the cross sections of the samples as shown in Fig. 10. At 70W (Fig. 10 a and b), the hardness of the Z65 sample ranges from 1169.72 HV to 1486.98 HV and the hardness of the Z75 sample ranges from 1248.98 HV to 1616.13 HV. The results show a decrease in hardness with increasing scanning speed of 70 W samples. In this study, the Z75-70W-120 mm/s sample did not produce prefabricated cracks under the same test conditions, so it will not be discussed here. At 90 W (Fig. 10 c and d), the hardness of the Z65

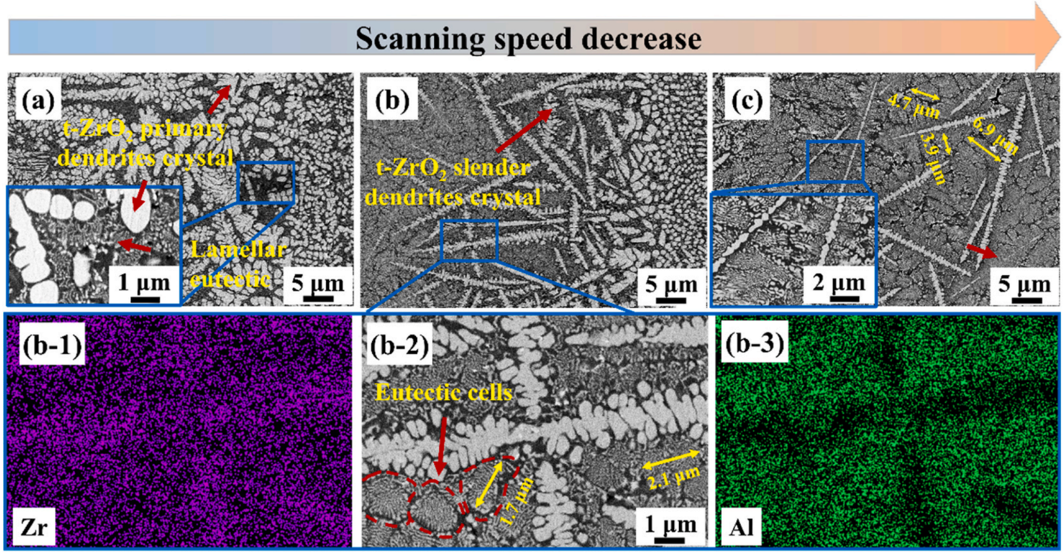

Fig. 8. SEM micrograph and EDS mapping of Z75 hypereutectic ceramic samples: (a) 120 mm/s, (b, b-2) 100 mm/s, (c) 80 mm/s, (b-1, b-3) Zr and Al EDS mapping of Figs. 8b–2.

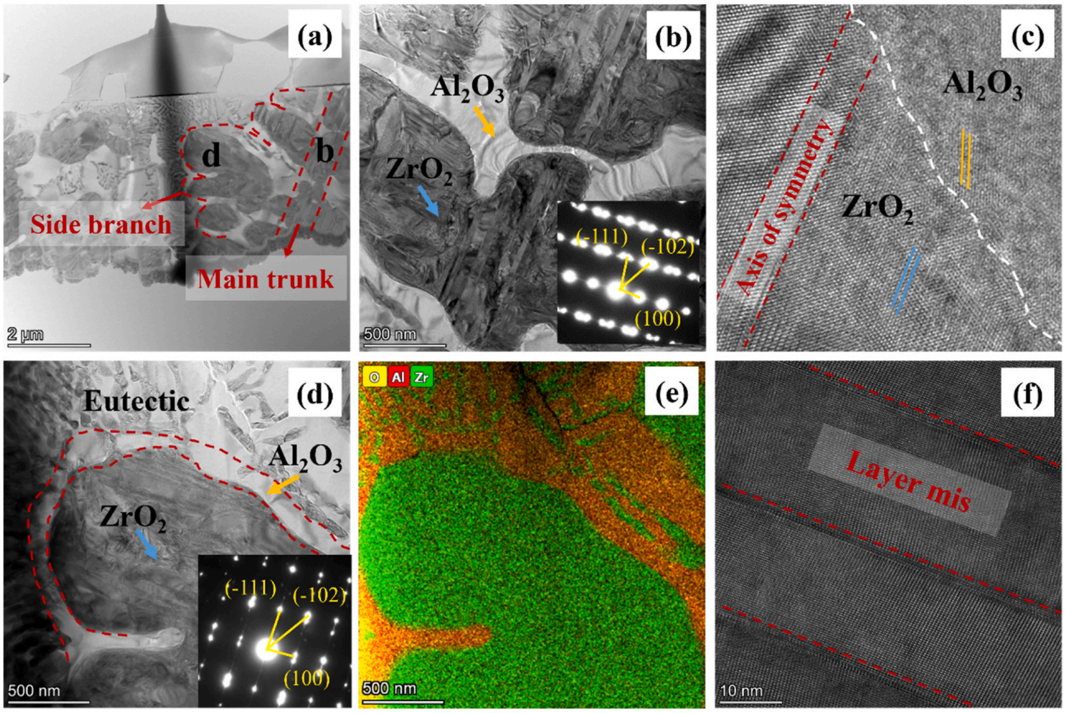

Fig. 9. (a) Thin-slice sample of Al_2O_3–ZrO_2 hypereutectic ceramic microstructure, (b) TEM bright-field (BF) image and SAED pattern showing the ZrO_2 dendrite, (c) at the Al_2O_3–ZrO_2 interface, (d) TEM bright-field (BF) image and SAED pattern showing the ZrO_2 dendrite, (e) EDXS image showing the surface distributions of elements, (f) TEM BF image showing the Al_2O_3–ZrO_2 hypereutectic with dislocation wall.

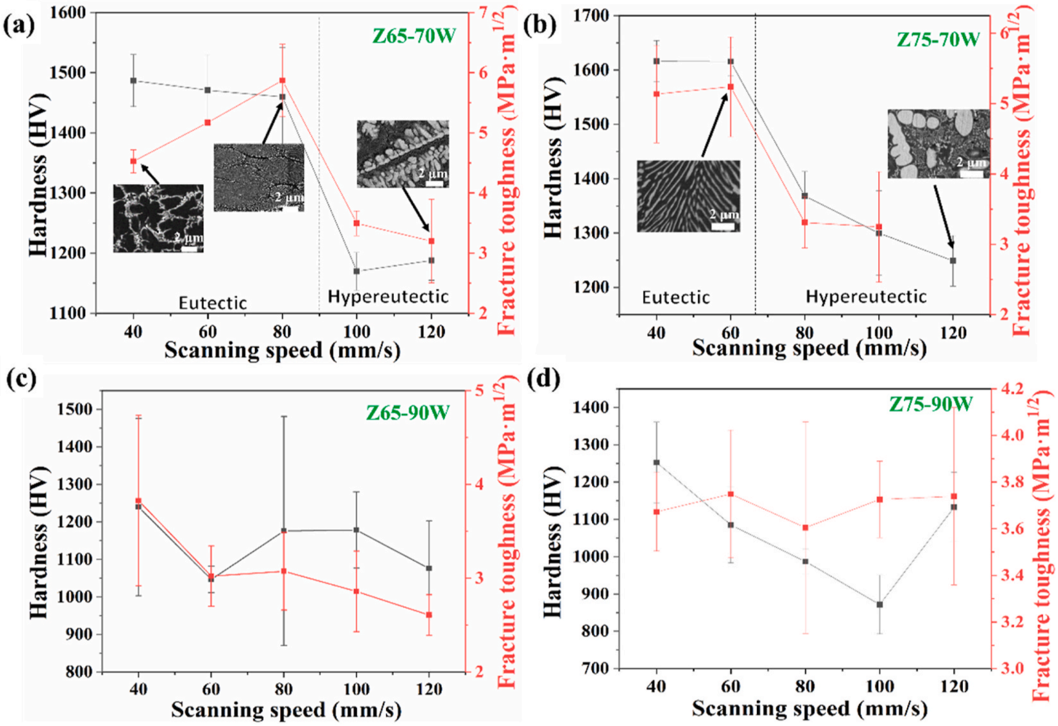

Fig. 10. Hardness and fracture toughness of (a) Z65-70W, (b) Z75-70W, (c)Z65-90W and (d) Z75-90W samples at different scanning speeds.

sample ranges from 1047.0 HV to 1240.06 HV and the hardness of Z75 sample ranges from 871.86 HV to 1252.56 HV. In addition, the hardness of the samples with eutectic structures is significantly higher than that of the hypereutectic samples. The maximum Vickers hardness observed in Z65 is 1486.98 HV at a scanning speed of 40 mm/s (Fig. 10a). Similarly, the maximum Vickers hardness measured in Z75 is 1616.13 HV at a scanning speed of 40 mm/s (Fig. 10b). This is attributed to the presence of numerous Al_2O_3 particles within the microstructure of the samples, which have a higher hardness (Figs. 6 and 7a).

The crack length caused by Vickers indentations can be used to calculate the fracture toughness (K_{IC}). At Z65-70W the fracture toughness initially increases and then decreases. Among them, the sample scanned at 80 mm/s has the highest fracture toughness 5.87 MPa·m$^{1/2}$, mainly due to its eutectic structure rather than the cracks and the pores (Fig. 10 and Fig. S2). Z75-70W samples also show that the fracture toughness of eutectic structure is higher than that of hypereutectic structure as shown in Fig. 10b. Therefore, it can be concluded that the different microstructures resulting from the different process parameters play a significant role in determining the mechanical properties of the samples. The main results are as follows: (1) The presence of hard Al_2O_3 particles significantly improves the hardness. (2) The uniform eutectic structure shows excellent hardness and fracture toughness. (3) The coarse deposition of ZrO_2 dendrites within the refined eutectic matrix reduces the toughening effect. This is observed as excessively fine primary eutectic structures in the hypereutectic sample as shown in the high magnification image in Fig. 10b.

Fig. 11 shows the Vickers indents at an applied load of 9.8 N on polished surfaces with different types of microstructures respectively. In the eutectic structure with Al_2O_3 particles, the crack propagation is much longer, and the crack bridges in the eutectic structure (Fig. 11a and a-1). A similar phenomenon occurs in the eutectic colony structure where cracks are deflected and bridged upon encountering ZrO_2 (Fig. 11b and b-1). In the hypereutectic structure, the cracks extend almost in a straight line within the eutectic region, while deflection and bridging occur in different degrees when encountering ZrO_2 dendrites (Fig. 11c and c-1).

From the perspective of crack propagation, the toughening effect can be observed in two aspects. (1) Crack bridging: From the crack path shown in Figs. 11a–1, it can be seen that the crack is terminated in the vicinity of the end region and then another parallel crack is formed below. This crack-bridging mechanism reduces the driving force for crack propagation and inhibits crack growth [36]. (2) Crack deflection: The initial crack deflects upon encountering a phase interface, as shown in Figs. 11b–1. The deflected crack path is indicated by the curved arrow.

4. Discussion

4.1. Microstructure evolution

The experimental findings revealed that a change in laser scan speed can significantly affect the microstructure of the samples produced. It can be seen from Figs. 4, 5, 7 and 8 that the microstructure of Al_2O_3–ZrO_2 ceramics shows obvious evolution under different scanning speeds. In order to better understand this evolutionary mechanism, the sequences of microstructural evolution are schematically illustrated in Fig. 12. At low laser energy density, the microstructure shows a typical hypereutectic structure, consisting of ZrO_2 dendrites and primary lamellar structure (Fig. 12a). With the increase of laser energy density, ZrO_2 dendrites gradually refined and eventually disappeared, while the surrounding lamellar structures continued to grow and resulted into a uniform eutectic colony structure, as shown in Fig. 12b. With a further increase of laser energy density, a band structure composed of coarse Al_2O_3 particles appeared in the eutectic colony structure (Fig. 12c). It is observed that the microstructure evolution of Al_2O_3–ZrO_2 ceramic is closely related to the structural evolution of its Al_2O_3 and ZrO_2 phases. Therefore, it is necessary to further study the evolution of Al_2O_3 and ZrO_2 phases.

4.2. ZrO_2 dendrites evolution

The changes in ZrO_2 dendrites during the microstructure evolution from hypereutectic structure to eutectic colony structure are shown in Fig. 13. As the laser energy density is lowered, a coarse primary phase of ZrO_2 begins to appear in the microstructure as shown in Fig. 13a. Simultaneously, the eutectic reaction of Al_2O_3 and ZrO_2 initiate, leading to the presence of eutectic structures surrounding the primary ZrO_2. As the energy density continued to increase, the ZrO_2 showed a clear trend growing along the main trunk, and the branches were refined into slender dendritic crystals (Fig. 13b). Because, for the intrinsic lattice structure, ZrO_2 has different crystal forms at different temperatures, and the phase transition of ZrO_2 is accompanied by volume expansion. When the energy density increases the local temperature increases, and the melt holds for a longer time because of the slow scanning speed, which leads to the formation of internal strain within the grain so that the overall ZrO_2 dendrite size gradually becomes longer in the main axis. In terms of the external environment, with the increase of energy density, the solidification rate and heat conduction effect during laser melting will also increase, which allows the side branches of ZrO_2 dendrite to form smaller sizes. Meanwhile, the surrounding eutectic structure gradually grows coarser boundaries, forming cellular structures attached to the ZrO_2 dendrite. At a higher laser energy density, the dendrite branches of ZrO_2 almost disappear. In the meantime, Zirconia dendrites continue to grow along the main axis, showing a morphology similar to beading (Fig. 13c). It is noteworthy that the eutectic structure grows from a small cellular structure to a rod-like structure, and its long axis is perpendicular to the main stem of the ZrO_2 dendrite. The eutectic colony structure with large size and irregular borders is eventually

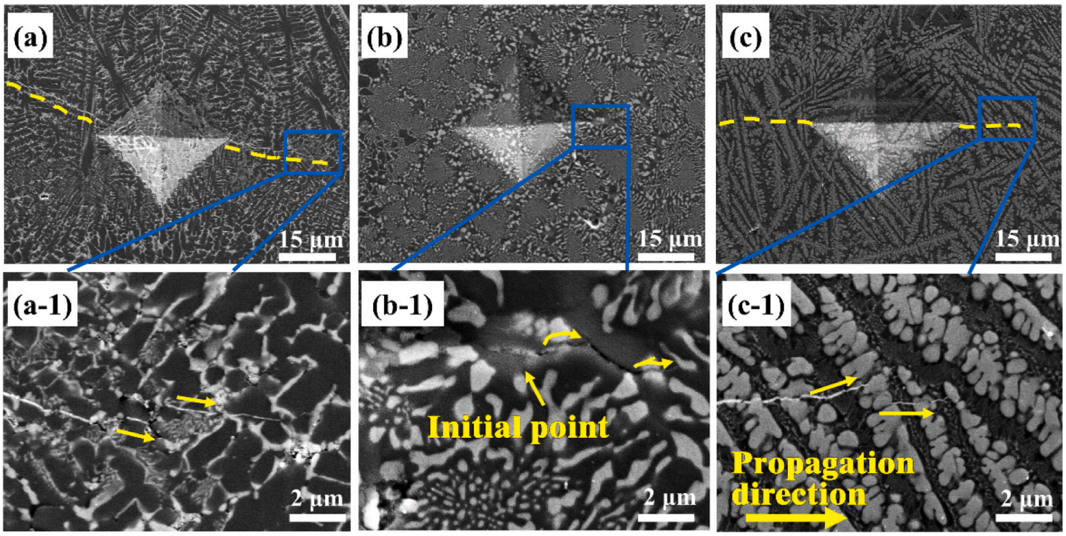

Fig. 11. Vickers indentation morphology on the polished surface and indentation cracks propagation pattern: (a, a-1) Al_2O_3 dendritic crystal, (b, b-1) eutectic, (c, c-1) ZrO_2 dendritic crystal.

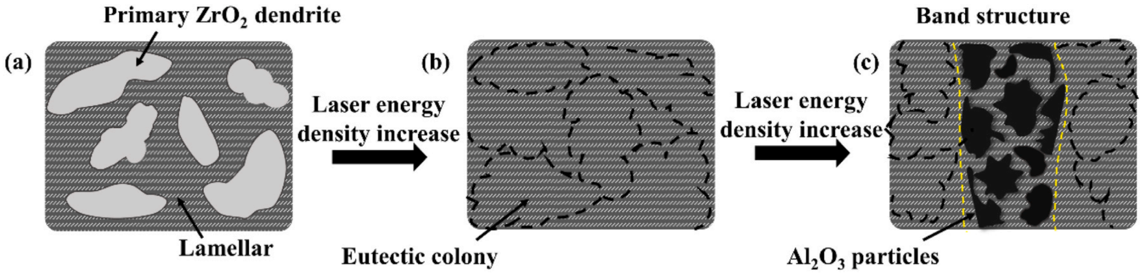

Fig. 12. (a) Typical hypereutectic structure, (b) typical eutectic structure, (c) eutectic structure with band structure.

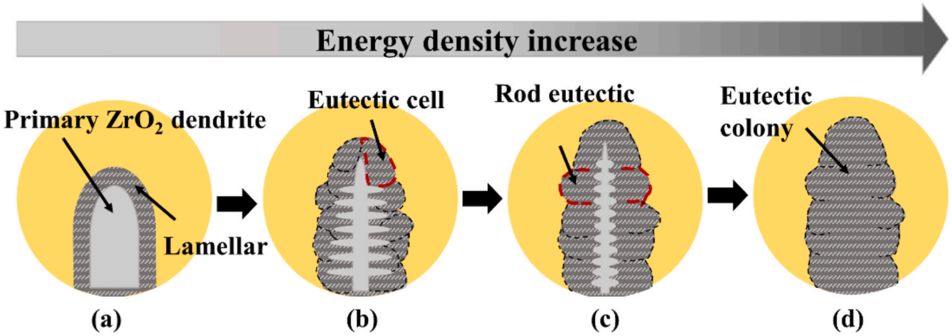

Fig. 13. Schematic illustration of the stage sequences of ZrO_2 dendrite evolution in Al_2O_3–ZrO_2 hypereutectic composition: (a) primary ZrO_2 dendrite and the peripheral lamellar structure, (b) dendrite is refined and the eutectic structure is cellular, (c) dendrites are further refined and rod-like eutectic grew, (d) dendrites disappear and form large eutectic colony.

produced when the ZrO_2 dendrites in the middle of the rod eutectic and boundaries between rod eutectic disappear, (Fig. 13d). Additionally, the long axis of the eutectic colony is parallel to the main stem of ZrO_2 dendrite. Finally, a typical eutectic structure is formed.

4.3. Al_2O_3 particles evolution

The microstructure of eutectic along with Al_2O_3 particles (Fig. 6) was further analyzed. This is assumed to be related to the undercooling. Previous studies have shown that the maximum thermal gradient exists near the boundary of the molten pool, and there is a lap zone with the previous molten pool, during that period the sample receives a higher energy [49–52]. When undercooling occurs, the solidification of the liquid phase is delayed, and the morphology and behavior of the solid/liquid interface are affected. The higher the degree of undercooling, the faster the movement of the solid/liquid interface, and the rapid progression of solidification. Under undercooling conditions, the solid/liquid interface exhibits phenomena such as uneven diffusion, displacement, and nucleation, ultimately leading to changes in the solidification morphology. The average undercooling $\triangle T$ at the interface is given by Ref. [53]:

$$\Delta T = T_E - T_L = \Delta T_D + \Delta T_r + \Delta T_k \tag{4}$$

where T_E is the eutectic temperature, T_L is the local interface temperature, and $\triangle T_D$, $\triangle T_r$, $\triangle T_k$ are the constitutional, curvature, and kinetic undercooling, respectively.

The constitutional undercooling ($\triangle T_D$) is caused by the solute concentration deviation from the initial concentration at the interface. At the boundary, the uneven distribution of heat flow leads to significant differences in thermal flux. This disparity in thermal flux can cause solute migration and aggregation, resulting in local oversaturation of solute at the boundary and leading to structural undercooling. As for the curvature undercooling ($\triangle T_r$), this is related to the increase in interface energy caused by the inclusion of a solid-liquid interface. The boundary of the liquid molten pool is the lap with the previously solidified layer. Therefore, this will produce a great curvature undercooling at the boundary. The increase of undercooling at the interface causes the growth interface single-phase instability and the appearance of the coarsening band structure. Based on this, the formation of primary dendritic Al_2O_3 and Al_2O_3–ZrO_2 eutectic colony of Z65-70W-40 mm/s sample can be well understood, as shown in Fig. 14.

The boundary of the molten pool is the lap with the previous molten pool, which exists a solid-liquid section with a higher undercooling. The primary phase of Al_2O_3 in this zone presents underdeveloped cellular, dendrites and ellipsoidal dendrite structures. ZrO_2 exists at the boundary of the Al_2O_3 cell separately and discontinuously. As it is near the center of the melting pool, the undercooling meets the condition of a eutectic reaction. The ZrO_2 phase forms nuclei on the surface of the Al_2O_3 dendrites. These nuclei serve as the starting points for the ZrO_2 crystals' growth. The ZrO_2 phase undergoes coupled growth after being nucleated. During coupled growth, the ZrO_2 phase continues to expand and interact with the surrounding Al_2O_3 dendrites. Subsequently, the cell structure is formed with alumina serving as the core and being surrounded by a eutectic structure. In the center of the molten pool, the condition is more stable as undercooling decreases, and the eutectic growth trend increases. Therefore, the eutectic reaction reaches completion and shows a uniformly distributed lamellar or eutectic colony structure.

5. Conclusions

In order to investigate the solidification behavior of Al_2O_3–ZrO_2 ceramics with a broader compositional landscape and understanding the "composition-microstructure" relationship during L-PBF and as result, tailor the mechanical properties, this study designed different material components and process parameters, prepared Al_2O_3–ZrO_2 hypereutectic ceramics via L-PBF, and analyzed their phase composition, microstructure evolution and mechanical properties. The mechanism of tissue evolution is discussed, and the major results are as follows:

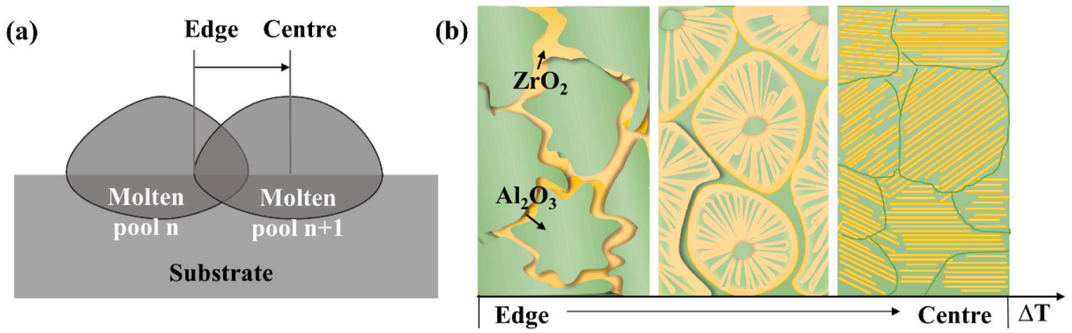

Fig. 14. (a) Molten pool location diagram, (b) schematic illustration of the stage sequences in Al_2O_3–ZrO_2 hypoeutectic - eutectic evolution.

(1) In terms of microstructure, the samples mainly formed a typical hypereutectic structure with a eutectic matrix and discrete distribution of ZrO_2 dendrites. However, eutectic structure can be obtained at a low scanning speed. With the decrease of the scanning speed, the microstructure changes from a hypereutectic structure to a eutectic structure. Further, there appeared a band structure composed of coarse Al_2O_3 particles in the eutectic colony structure.

(2) The scanning speed can significantly influence the evolution of ZrO_2 dendrites in Al_2O_3–ZrO_2 hypereutectic ceramics. With the increase of laser energy density, the ZrO_2 gradually changes from coarse primary morphology into slender dendrite, while the eutectic structure between dendrites changes from lamellar structure to eutectic colony structure, and the ZrO_2 dendrites disappear.

(3) In terms of mechanical properties, the sample with alumina particles in their microstructure exhibits the highest hardness of 1616.13 HV, and the one with uniform eutectic microstructure has the highest fracture toughness of 5.87 $MPa \cdot m^{1/2}$. In general, the presence of ZrO_2 dendrites enhance the fracture toughness of Al_2O_3–ZrO_2 ceramics. However, undesirably the high scanning speed will make the surrounding eutectic matrix too fine while obtaining ZrO_2 dendrites, leading to a fracture toughness lower than that of relatively rough and coarser eutectic structure. Therefore, in order to obtain superior mechanical properties, it is necessary to precisely regulate and control the growth of eutectic matrix and ZrO_2 dendrites.

Declaration of competing interest

The author(s) declared no potential conflicts of interest with respect to the research, author-ship, and/or publication of this article.

Acknowledgement

This work was supported by the National Natural Science Foundation of China (Grant No. 52005262) and National Key Research and Development Program of China (2022YFB4600800).

Appendix A. Supplementary data

Supplementary data to this article can be found online at https://doi.org/10.1016/j.smmf.2024.100048.

References

[1] J. Chai, Y. Zhu, Z. Wang, T. Shen, Y. Liu, L. Niu, S. Li, C. Yao, M. Cui, C. Liu, Microstructure and mechanical properties of SPS sintered Al_2O_3–ZrO_2 (3Y)–SiC ceramic composites, Mat. Sci. Eng. A-Struct. 781 (2020) 139197.

[2] D. Galusek, J. Sedláček, J. Chovanec, M. Michálková, The influence of MgO, Y_2O_3 and ZrO_2 additions on densification and grain growth of submicrometre alumina sintered by SPS and HIP, Ceram. Int. 41 (8) (2015) 9692–9700.

[3] W. Huang, Y. Zhang, J. Lu, L. Gao, F. Zhang, J. Chen, M. Omran, G. Chen, Effect of sintering time on the microstructure and stability of Al_2O_3–ZrO_2 composite powders under microwave-assisted sintering, Ceram. Int. 49 (6) (2023) 8993–8999.

[4] J. Zhang, T. Zhu, S. Sang, Z. Xie, Y. Li, N. Liao, L. Pan, J. Dai, Optimization of microstructure and mechanical properties of oscillatory pressure sintered ZrO_2–Al_2O_3-SiCp ceramics, Ceram. Int. 48 (6) (2022) 7512–7521.

[5] X. Xu, Y. Yang, X. Wang, X. Su, J. Liu, Low-temperature preparation of Al_2O_3-ZrO_2 nanoceramics via pressureless sintering assisted by amorphous powders, J. Alloys Compd. 783 (2019) 806–812.

[6] M.W. Khalid, Y.I. Kim, M.A. Haq, D. Lee, B.S. Kim, B. Lee, Microwave hybrid sintering of Al_2O_3 and Al_2O_3–ZrO_2 composites, and effects of ZrO_2 crystal structure on mechanical properties, thermal properties, and sintering kinetics, Ceram. Int. 46 (7) (2020) 9002–9010.

[7] X. Cao, H. Su, F. Guo, X. Tan, L. Cao, Directionally solidified Al_2O_3/GAP eutectic ceramics by micro-pulling-down method, in: AIP Conference Proceedings, AIP Publishing, 2016.

[8] X. Wang, N. Zhang, Y. Zhong, B. Jiang, L. Lou, J. Zhang, J. Wang, Microstructure evolution and crystallography of directionally solidified Al_2O_3/$Y_3Al_5O_{12}$ eutectic ceramics prepared by the modified Bridgman method, J. Mater. Sci. Technol. 35 (9) (2019) 1982–1988.

[9] S. Wang, Z. Chu, J. Liu, Microstructure and mechanical properties of directionally solidified Al_2O_3/$GdAlO_3$ eutectic ceramic prepared with horizontal high-frequency zone melting, Ceram. Int. 45 (8) (2019) 10279–10285.

[10] H. Su, Q. Ren, J. Zhang, K. Wei, B. Yao, W. Ma, G. Fan, M. Guo, L. Liu, H. Bai, H. Fu, Microstructures and mechanical properties of directionally solidified Al_2O_3/$GdAlO_3$ eutectic ceramic by laser floating zone melting with high temperature gradient, J. Eur. Ceram. Soc. 37 (4) (2017) 1617–1626.

[11] A. Paolini, S. Kollmannsberger, E. Rank, Additive manufacturing in construction: a review on processes, applications, and digital planning methods, Addit. Manuf. 30 (2019) 100894.

[12] F. Verga, M. Borlaf, L. Conti, K. Florio, M. Vetterli, T. Graule, M. Schmid, K. Wegener, Laser-based powder bed fusion of alumina toughened zirconia, Addit. Manuf. 31 (2020) 100959.

[13] Y. Zhang, A. Bandyopadhyay, Direct fabrication of compositionally graded Ti-Al_2O_3 multi-material structures using Laser Engineered Net Shaping, Addit. Manuf. 21 (2018) 104–111.

[14] S. Li, K. Zhang, Z. Yan, T. Liu, Z. Zhu, Z. Xiong, Z. Zou, J. Li, W. Liao, Effect of Nb addition on the microstructure and mechanical properties of additively manufactured Ti_2AlC MAX-phase ceramic matrix composites, Addit. Manuf. 67 (2023) 103488.

[15] G. Fan, H. Su, J. Zhang, M. Guo, H. Yang, H. Liu, E. Wang, L. Liu, H. Fu, Microstructure and cytotoxicity of Al_2O_3-ZrO_2 eutectic bioceramics with high mechanical properties prepared by laser floating zone melting, Ceram. Int. 44 (15) (2018) 17978–17985.

[16] H. Liu, H. Su, Z. Shen, H. Jiang, D. Zhao, Y. Liu, Y. Guo, X. Li, M. Guo, J. Zhang, L. Liu, H. Fu, Formation mechanism and roles of oxygen vacancies in melt-grown Al_2O_3/$GdAlO_3$/ZrO_2 eutectic ceramic by laser 3D printing, J. Adv. Ceram. 11 (11) (2022) 1751–1763.

[17] D. Zhao, D. Wu, J. Shi, F. Niu, G. Ma, Microstructure and mechanical properties of melt-grown alumina-mullite/glass composites fabricated by directed laser deposition, J. Adv. Ceram. 11 (1) (2021) 75–93.

[18] H. Amano, T. Ishimoto, K. Hagihara, R. Suganuma, K. Aiba, S.-H. Sun, P. Wang, T. Nakano, Impact of gas flow direction on the crystallographic texture evolution in laser beam powder bed fusion, Virtual Phys. Prototyp. 18 (1) (2023) e2169172.

[19] O. Gokcekaya, T. Ishimoto, T. Todo, P. Wang, T. Nakano, Influence of powder characteristics on densification via crystallographic texture formation: Pure tungsten prepared by laser powder bed fusion, Addit. Manuf. Ltr. 1 (2021) 100016.

[20] P. Wang, M.L.S. Nai, F.L. Ng, A. Tan, W.J. Sin, M.H. Goh, Y. Maruno, Revealing mechanisms underlying powder reusability of Ti-48Al-2Cr-2Nb intermetallic in electron beam powder bed fusion process, Addit. Manuf. 59 (2022) 103155.

[21] M. Cagirici, P. Wang, F.L. Ng, M.L.S. Nai, J. Ding, J. Wei, Additive manufacturing of high-entropy alloys by thermophysical calculations and in situ alloying, J. Mater. Sci. Technol. 94 (2021) 53–66.

[22] P. Wang, M.H. Goh, Q. Li, M.L. S Nai, J. Wei, Effect of defects and specimen size with rectangular cross-section on the tensile properties of additively manufactured components, Virtual Phys. Prototyp. 15 (2020) 251–264.

[23] S.S. Hossain, K. Lu, Recent progress of alumina ceramics by direct ink writing: Ink design, printing and post-processing, Ceram. Int. 49 (7) (2023) 10199–10212.

[24] Z. Liu, C. Ma, Z. Chang, P. Zhao, Y. Zhang, Q. Wu, F. Li, Formation mechanism and quantitative analysis of pores in Al_2O_3-ZrO_2 ceramic different structures by laser additive manufacturing, Ceram. Int. 49 (10) (2023) 16099–16109.

[25] H. Liu, H. Su, Z. Shen, D. Zhao, Y. Liu, Y. Guo, J. Zhang, L. Liu, H.Z. Fu, Insights into high thermal stability of laser additively manufactured Al_2O_3/$GdAlO_3$/ZrO_2 eutectic ceramics under high temperatures, Addit. Manuf. 48 (2021) 102425.

[26] S. Yan, Y. Huang, D. Zhao, F. Niu, G. Ma, D. Wu, 3D printing of nano-scale Al_2O_3-ZrO_2 eutectic ceramic: Principle analysis and process optimization of pores, Addit. Manuf. 28 (2019) 120–126.

[27] D. Wu, X. Yu, Z. Zhao, G. Ma, C. Zhou, B. Zhang, G. Ren, F.Y. Niu, One-step additive manufacturing of TiCp reinforced Al_2O_3-ZrO_2 eutectic ceramics composites by laser directed energy deposition, Ceram. Int. 49 (8) (2023) 12758–12771.

[28] Z. Chen, X. Sun, Y. Shang, K. Xiong, Z. Xu, R. Guo, S. Cai, C. Zheng, Dense ceramics with complex shape fabricated by 3D printing: a review, J. Adv. Ceram. 10 (2021) 195–218.

[29] D. Wu, X. Yu, Z. Zhao, G. Ma, C. Zhou, B. Zhang, G.H. Ren, J. Han, H. Wang, F. Y. Niu, Direct additive manufacturing of TiCp reinforced Al_2O_3-ZrO_2 eutectic functionally graded ceramics by laser directed energy deposition, J. Eur. Ceram. Soc. 43 (6) (2023) 2718–2723.

[30] H. Liu, H. Su, Z. Shen, D. Zhao, Y. Liu, Y. Guo, M. Guo, J. Zhang, L. Liu, H.Z. Fu, Preparation of large-size Al_2O_3/$GdAlO_3$/ZrO_2 ternary eutectic ceramic rod by laser directed energy deposition and its microstructure homogenization mechanism, J. Mater. Sci. Technol. 85 (20) (2021) 218–223.

[31] S. Yan, D. Wu, F. Niu, Y. Huang, N. Liu, G. Ma, Effect of ultrasonic power on forming quality of nano-sized Al_2O_3-ZrO_2 eutectic ceramic via laser engineered net shaping (LENS), Ceram. Int. 44 (1) (2018) 1120–1126.

[32] S. Yan, D. Wu, F. Niu, G. Ma, R. Kang, Al_2O_3-ZrO_2 eutectic ceramic via ultrasonic-assisted laser engineered net shaping, Ceram. Int. 43 (17) (2017) 15905–15910.

[33] Z. Shen, H. Su, M. Yu, Y. Guo, Y. Liu, D. Zhao, H. Jiang, P. Yang, M.Q. Yang, Z. Zhang, M. Guo, W. Ren, Large-size complex-structure ternary eutectic ceramic fabricated using laser powder bed fusion assisted with finite element analysis, Addit. Manuf. 72 (2023) 103627.

[34] S. Yan, D. Wu, G. Ma, F. Niu, R. Kang, D. Guo, Formation mechanism and process optimization of nano Al_2O_3-ZrO_2 eutectic ceramic via laser engineered net shaping (LENS), Ceram. Int. 43 (2017) 14742–14747.

[35] H. Su, H. Liu, H. Jiang, Z. Shen, Q. Chen, M. Yu, D. Zhao, X. Li, D. Dong, Z. Zhang, One-step preparation of melt-grown Al_2O_3/$GdAlO_3$/ZrO_2 eutectic ceramics with large size and irregular shape by directed energy deposition, Addit. Manuf. 70 (2023) 103563.

[36] D. Wu, J. Shi, F. Niu, G. Ma, C. Zhou, B. Zhang, Direct additive manufacturing of melt growth Al_2O_3-ZrO_2 functionally graded ceramics by laser directed energy deposition, J. Eur. Ceram. Soc. 42 (6) (2022) 2957–2973.

[37] D. Wu, J. San, F. Niu, D. Zhao, Y. Huang, G. Ma, Directed laser deposition of Al_2O_3-ZrO_2 melt-grown composite ceramics with multiple composition ratios, J. Mater. Sci. 55 (2020) 6794–6809.

[38] K. Song, J. Zhang, X. Lin, L. Liu, W. Huang, Microstructure and mechanical properties of Al_2O_3/YAl_5O_{12}/ZrO_2 hypereutectic directionally solidified ceramic prepared by laser floating zone, J. Eur. Ceram. Soc. 34 (12) (2014) 3051–3059.

[39] H.J. Su, J. Zhang, Y.F. Deng, L. Liu, H.Z. Fu, Growth and characterization of nanostructured Al_2O_3/YAG/ZrO_2 hypereutectics with large surfaces under laser rapid solidification, J. Cryst. Growth 312 (24) (2010) 3637–3641.

[40] Z. Xiong, K. Zhang, Z. Zhu, T. Liu, Y. Zhang, S. Li, W. Liao, Effect of laser focus shift on the forming quality, microstructure and mechanical properties of additively manufactured Al_2O_3–ZrO_2 eutectic ceramics, Ceram. Int. 49 (22) (2023) 35948–35962.

[41] Z. Xiong, K. Zhang, T. Liu, Z. Zhu, H. Wei, Z. Zou, W. Liao, Role of scanning speed on the microstructure and mechanical properties of additively manufactured Al_2O_3–ZrO_2, J. Am. Ceram. Soc. 106 (12) (2023) 7760–7775.

[42] N. Kazantseva, P. Krakhmalev, M. Thuvander, I. Yadroitsev, N. Vinogradova, I. Ezhov, Martensitic transformations in Ti-6Al-4V (ELI) alloy manufactured by 3D Printing, Mater. Char. 146 (2018) 101–112.

[43] I.S. Medeiros, E.R.M. Andreeta, A.C. Hernandes, Al_2O_3/$GdAlO_3$ eutectic fibers of high modulus of rupture produced by the laser heated pedestal growth technique, J. Mater. Sci. 42 (2007) 3874–3877.

[44] H. Liu, H. Su, Z. Shen, E. Wang, D. Zhao, M. Guo, J. Zhang, L. Liu, H. Fu, Direct formation of Al_2O_3/$GdAlO_3$/ZrO_2 ternary eutectic ceramics by selective laser melting: microstructure evolutions, J. Eur. Ceram. Soc. 38 (15) (2018) 5144–5152.

[45] L. Fu, X. Fu, G. Chen, W. Han, W. Zhou, Tailoring the morphology in Y_2O_3 doped melt-grown Al_2O_3/ZrO_2 eutectic ceramic, Scripta Mater. 129 (2017) 20–24.

[46] G. Ma, S. Yan, F. Niu, Y. Zhang, D. Wu, Microstructure and mechanical properties of solid Al_2O_3-ZrO_2(Y_2O_3) eutectics prepared by laser engineered net shaping, J. Laser Appl. 29 (2017) 022305.

[47] D. Wu, Y. Zhang, F. Niu, G. Ma, R. Kang, Influence of laser power on the forming quality of Al_2O_3-ZrO_2 eutectic ceramic, Rare Met. Mater. Eng. 43 (11) (2014) 2814–2818.

[48] W. Ma, J. Zhang, H. Su, G. Fan, M. Guo, L. Liu, H. Fu, Phase growth patterns for Al_2O_3/$GdAlO_3$ eutectics over wide ranges of compositions and solidification rates, J. Mater. Sci. Technol. 65 (2021) 89–98.

[49] H. Liu, H. Su, Z. Shen, D. Zhao, Y. Liu, M. Guo, Y. Guo, J. Zhang, L. Liu, H. Fu, Effect of scanning speed on the solidification process of Al_2O_3/$GdAlO_3$/ZrO_2 eutectic ceramics in a single track by selective laser melting, Ceram. Int. 45 (14) (2019) 17252–17257.

[50] Z. Fan, Y. Zhao, Q. Tan, N. Mo, M.X. Zhang, M. Lu, H. Huang, Nanostructured Al_2O_3-YAG-ZrO_2 ternary eutectic components prepared by laser engineered net shaping, Acta Mater. 170 (2019) 24–37.

[51] F. Niu, D. Wu, G. Ma, J. Wang, M. Guo, B. Zhang, Nanosized microstructure of Al_2O_3-ZrO_2(Y_2O_3) eutectics fabricated by laser engineered net shaping, Scripta Mater. 95 (2015) 39–41.

[52] Q. Chen, G. Guillemot, C.A. Gandin, M. Bellet, Numerical modelling of the impact of energy distribution and Marangoni surface tension on track shape in selective laser melting of ceramic material, Addit. Manuf. 21 (2018) 713–723.

[53] C. Cui, J. Zhang, T. Xue, L. Liu, H. Fu, Effect of solidification rate on microstructure and solid/liquid interface morphology of Ni-11.5 wt. % Si eutectic alloy, J. Mater. Sci. Technol. 31 (3) (2015) 280–284.